Subpicosecond Imaging System Based on Electro-Optic Effect

Ultrafast electro-optic (EO) sampling was first demonstrated in 1982[1] and has since become a valuable tool for testing optoelectronic and electronic devices and materials.[2] Conventional EO sampling of weak electric fields employs a tightly focused, pulsed-laser probe beam to measure electric-field-induced birefringence in an EO crystal; hence, it is referred to as "point" sampling.

Densely packed analog and digital devices make it necessary to probe many nodes simultaneously. Meyer and Mourou[3] first demonstrated electric field mapping by scanning an area using a point sampler. Mertin[4] reviews the development of two-dimensional field measurement technologies including an automated scanning point sampler. Two groups studying photoconductive switches[5,6] pioneered the use of EO imaging, by mapping the field strength with a detector array. Their work differs from the present in that their devices exhibited high fields and were adequately described with 200-ps temporal resolution.

An EO sampling system capable of imaging the voltage distribution over a rectangular region is described. It is comparable to an ultrafast sampling oscilloscope having more than 180,000 channels. This analysis focuses on techniques that take advantage of the speed and convenience of a charge-coupled-device (CCD) sensor while overcoming its limited dynamic range.

System Descriptions

EO sampling requires a pulsed (or gated) laser source to probe the response of the device to the applied transient. Our lab uses a mode-locked Coherent Mira 900 Ti:sapphire laser. It produces a 76-MHz train of linearly polarized, ≈100-fs FWHM pulses, tuned to ≈800 nm. Devices tested in our lab generally include a photoconductive switch that is excited with a fraction of the pulsed beam, thus triggering the measurement and eliminating electrical jitter.

In a point sampler,[2] the EO crystal may be either the device substrate (e.g., GaAs devices) or on an external probe. A linearly polarized optical probe pulse enters the crystal through the first surface. In transmissive sampling, the probe is transmitted at the second surface after a single pass, whereas in reflective sampling, it is reflected, passing through the crystal a second time. The beam exits the crystal and is passed through a compensator or wave plate to introduce a static polarization bias. The bias is adjusted so that in the absence of an electric field, the probe is circularly polarized at the input of an analyzer, thus giving maximum sensitivity and linearity when a field is applied. The analyzer separates the beam into orthogonal polarization components, which are measured by a pair of detectors connected to a differential lock-in amplifier. Signal-to-noise improvements are obtained when the signal is modulated at frequencies approaching the laser $1/f$ noise floor.

Figure 69.31 depicts the imaging system hardware. Reflective sampling was chosen because it doubles system sensitivity, although transmissive sampling is also possible. The laser source is directed through a high-speed modulator followed by a variable-intensity beam splitter consisting of a half-wave plate and polarizing beam splitter. The horizontally polarized "probe" beam is directed back through the polarizer, then into a spatial filter and beam expander. The vertically polarized "excitation" beam passes through a variable-length optical delay and into a fiber coupler.

The probe beam is split into two beams in a small, rigid interferometer. The device-under-test (DUT) is mounted in the device "leg" of the interferometer, and a mirror is installed in the reference "leg." The beams pass through a polarizing filter and relay lens to create an interference pattern at the camera. The beam splitter in the interferometer is an uncoated, ≈3-mm-thick, BK-7 wedged window. The first surface of the window is aligned at Brewster's angle to eliminate multiple reflections and maximize transmitted intensity. The reference
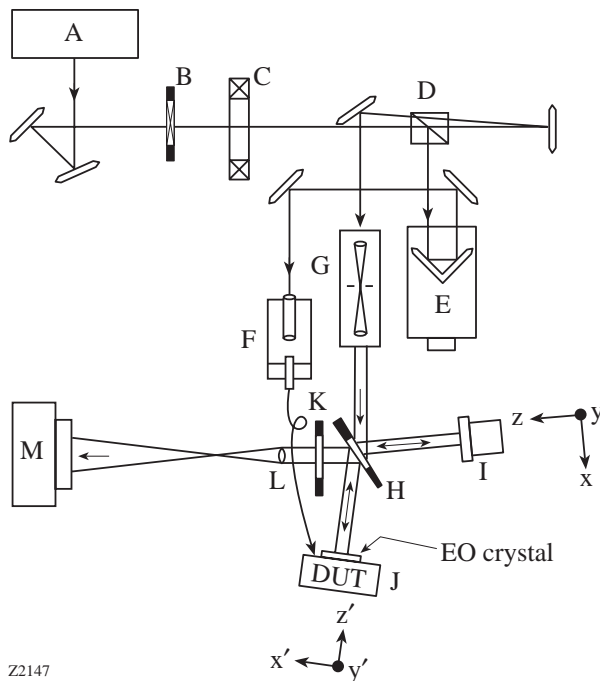
Z2147

Figure 69.31

Imaging system hardware: (A) Ti:sapphire laser, (B) high-frequency modulator, (C) half-wave plate, (D) polarizing beam splitter, (E) optical delay stage, (F) excitation beam fiber coupler, (G) spatial filter and probe beam expander, (H) wedged beam splitter, (I) reference mirror on piezoelectric actuator, (J) EO crystal on DUT, (K) polarizing filter, (L) relay lens and aperture, and (M) CCD camera.

mirror is mounted on a piezoelectric actuator, which is used to modulate the length of the reference leg. The DUT is mounted on a stationary structure. Each leg has adjustments for static alignment.

As in point sampling, the electric fields on the DUT are measured by using the linear EO, or Pockels, effect. A propagating electrical transient is launched on the DUT when an optical excitation pulse is applied to a biased, photoconductive switch. An EO crystal having a high-reflectivity (HR) coating on one side covers the region of interest with the coating in intimate contact with the DUT. "Fringing" E-fields caused by the propagating transient couple into the crystal to produce a temporally and spatially variant refractive index.

The EO-induced index perturbation in the crystal alters the phase of the linearly polarized optical probe as it traverses the device leg of the interferometer. When recombined with an unperturbed reference beam, an intensity pattern results that corresponds to phase differences between the two legs of the interferometer. If the reference beam is static, then changes in

intensity at each point can be attributed to spatial phase variations in the crystal induced by the EO effect.

A video camera (DVC Corp., DVC-0A) having a low-noise, frame-transfer charge-coupled device (CCD) (Texas Instruments, TC-245) records the intensity pattern created by the interferometer. The analog camera output is digitized by a frame grabber (Matrox Corp., Pulsar) and stored on a personal computer (Pentium 133-MHz, PCI bus). Timing control for modulation uses custom-built electronics (see **Modulation** section).

Spatial resolution of the system is determined by the active image area and number of discrete pixels in the image sensor. Image (de)magnification can be adjusted by altering the position of the relay lens and camera.

The CCD has 755 (8.5-μm) pixels horizontally (H) and 242 (19.75-μm) pixels vertically (V) for an active area of 6.4 mm (H) × 4.8 mm (V). Typical magnification is 4:1, giving a measurement area of 1.6 mm (H) × 1.2 mm (V). The resulting spatial resolution is 2.13 μm (H) × 4.9 μm (V), which is comparable to point sampling. If desired, cylindrical lenses or prisms could be used to correct the pixel aspect ratio.

It is possible to increase optical magnification to 8:1, then digitally average 2 × 2-pixel cells to obtain 4:1 effective magnification. This would reduce noise by 1/2; however, it may prove disadvantageous since more photons from the excitation source will be collected by the sensor [see also **Interferometer Operation** section].

Important distinctions exist between the imager and scanning point samplers. The imaged nodes must lie within a finite rectangular region, whereas a scanning system can probe random points over an extended area. Furthermore, the imager measures all nodes simultaneously, whereas a scanning sampler probes one node at a time.

Electro-Optic Interferometer

We present the reasons for choosing an interferometer and discuss its operation. We begin by mathematically describing the EO effect, and the relationship between the voltages present on the DUT, fringing fields coupled into the crystal, and resulting phase delay experienced by the optical probe. We then use this information to estimate the temporal resolution of the system. Following this discussion, we analyze the design in Fig. 69.31 to estimate the expected system sensitivity.

The refractive index in an EO crystal is altered in the presence of an electric field. The perturbed index n' is dependent on the field-free index n, field strength E, and Pockels coefficients r. By applying the techniques of Ref. 7 to x-cut LiTaO$_3$ (<3 m> point group), a material commonly used for EO sampling, we find (neglecting terms quadratic in field strength E_y)

$$n'_y = n_y - \frac{n_y^3}{2}\left(r_{22}E_y + r_{13}E_z\right) = n_y + \Delta n_y, \qquad (1a)$$

$$n'_z = n_z - \frac{n_z^3}{2}\left(r_{33}E_z\right) = n_z + \Delta n_z. \qquad (1b)$$

Numeric subscripts are indices of the tensor elements, and y, z subscripts are direction vectors in crystalline coordinates; z is parallel to the optic axis. These equations show that the refractive index along y is influenced by the electric fringing fields directed along both y and z, whereas the index along z is influenced only by fringing fields along z. It is also evident that the optical probe polarization must be aligned to measure the desired refractive index perturbation, while the optic axis of the crystal must be aligned on the DUT such that the fringing fields of interest maximize the index perturbation.

If we substitute values for LiTaO$_3$[7] into Eqs. (1a) and (1b), we find that $\Delta n_z \approx 4.4 \, \Delta n_y$, and the contribution from E_y is negligible. In point sampling, it is common (and convenient) to measure the induced birefringence, which is the difference in index perturbation along z and y, or

$$\Delta n_{zy} = \Delta n_z - \Delta n_y \approx \Delta n_z / 1.3.$$

Since the refractive index change along z is greater than that along y and greater than the induced birefringence, system sensitivity will be maximized by measuring Δn_z. An interferometer was chosen for this purpose. [Note: EO materials from other point groups (e.g., ZnTe, <43 m>) have greater sensitivity when the induced birefringence is measured.]

Having determined that we wish to measure the refractive index perturbation using an interferometer, we must consider how it will be used. An interferometer is sensitive to phase delays imposed on a propagating optical wavefront, which in our case is the probe beam. As an optical beam traverses a dielectric material, it suffers a phase delay $\Delta\Gamma$, determined by the refractive index n, wavelength λ, and material thickness X:

$$\Delta\Gamma = \int_0^X \frac{2\pi}{\lambda} n(x)\, dx. \qquad (2)$$

We showed above that the refractive index was dependent upon the electric fringing field, but we must also consider that the fringing field is not uniform throughout the thickness of the material. As a result, the refractive index is a function of depth x, determined by the penetration depth of the fringing field into the crystal.

Substituting Eq. (1b) into Eq. (2), we obtain a static phase delay component Γ_0 (independent of E fields):

$$\Gamma_0 = \frac{2\pi}{\lambda} n_z X, \qquad (3a)$$

and a dynamic phase delay attributed to the EO effect $\Delta\Gamma_{EO}$. The interferometer measures $\Delta\Gamma_{EO}$, given by

$$\Delta\Gamma_{EO} = \frac{\pi}{\lambda} n_z^3 \, r_{33} \int_0^X E_z(x)\, dx. \qquad (3b)$$

The E-field distribution within the crystal depends upon the test structure. For this example, consider a coplanar waveguide on which we wish to probe the E-field at the center of the gap g. In general, if a superstrate having the same relative dielectric constant as the substrate (ε_{sub}) is placed on a coplanar structure, we would expect the fringing fields in the superstrate to be confined to a depth comparable to the gap separating device features. When the superstrate is the EO crystal (dielectric = ε_{EO}), the depth of the fringing field, g', is dependent upon the ratio of the two dielectric constants; the confinement depth becomes $g' \cong g \, \varepsilon_{sub}/\varepsilon_{EO}$. The field strength decreases rapidly inside the crystal, so we approximate the integral with the product $E_z^{surface} g'$, where $E_z^{surface}$ is the transverse E-field magnitude at the surface of the crystal. We then obtain

$$\Delta\Gamma_{EO} \cong \frac{\pi}{\lambda} \, n_z^3 \, r_{33}\left(\frac{\varepsilon_{sub} \, g E_z^{surface}}{\varepsilon_{EO}} \right), \qquad (3c)$$

or in words, the measured phase change at any point is proportional to the E-field at that point. The voltage on the gap V^{gap} is the product of the gap and the E-field:

$$V^{gap} = g \, E_z^{surface}. \qquad (3d)$$

Note that for a given value of $\Delta\Gamma_{EO}$, the voltage is independent of the gap, whereas the field depends upon the gap. This can be understood by considering that a device having a larger gap has deeper fringing-field penetration in the crystal. The fields have a longer interaction length with the probe; hence, the field required to produce a given phase change is reduced.

Temporal resolution of the system is determined by the largest of (1) response time of the EO material, or (2) probe-pulse duration convolved with the fringing fields profile; this convolution is approximately equal to the sum of the pulse FWHM and the time of flight t_{fl} of an infinitely short pulse through the fringing fields. The EO response is limited by phonon resonance and for LiTaO$_3$ is of the order of 10^{-14} s.[8] The probe pulse is $\approx$100-fs FWHM and can be reduced to $\approx$50-fs FWHM using a pulse compressor. The optical path length through the fringing fields is $pl = \left(2\,n\,g\,\varepsilon_{sub}/\varepsilon_{EO}\right)$. Time of flight $t_{fl} = pl/c$, with c = speed of light in vacuum. For a coplanar waveguide fabricated on silicon ($\varepsilon_{sub} = 11.9$), having $g = 10\ \mu m$, and LiTaO$_3$ ($n \approx 2.2$, $\varepsilon_{EO} = 43$), we find $t_{fl} \approx 40$ fs. From these values, we expect (temporal resolution) $\approx$ (pulse FWHM + t_{fl}) = 140 fs, well below 1 ps.

Interferometer Operation

Now that we have described how Pockels effect alters the phase of an optical probe beam, we discuss the interferometer in detail. We begin with its intensity transfer function and discuss the ideal case. We then consider factors that cause deviations from ideal that reduce system sensitivity, and estimate their magnitude. Finally, we consider how to optimize system sensitivity given these constraints.

The normalized intensity measured by the detector, $I_d = I_{out}/I_{ref}$, is the ratio of the output intensity from the interferometer to the intensity present in the reference leg:

$$I_d \equiv \frac{I_{out}}{I_{ref}} = (1+\alpha) + 2\sqrt{\alpha}\,\cos(\delta) + b. \qquad (4)$$

I_d depends on $\alpha = I_{DUT}/I_{ref}$, the normalized intensity in the device leg, the phase difference δ between the E-field of the optical probe in each leg, and normalized background illumination b. Using Eqs. (3a) and (3c) to expand δ, we get

$$\delta = 2\left(\Gamma_0 + \Delta\Gamma_{EO}\right) \equiv 2\Gamma, \qquad (5)$$

where Γ_0 was redefined to include both the static phase difference governed by the differing lengths of the interferom-

eter legs, as well as the static phase delay of the EO crystal. The factor of 2 results from using reflective sampling. The probe passes through the fringing field two times, accumulating twice the phase delay.

In an ideal interferometer $\alpha = 1$ and $b = 0$, and Eq. (4) reduces to

$$I_d \propto \cos^2(\Gamma), \qquad (6)$$

which is also the intensity transfer function used to describe point sampling. As a result, all modulation and detection principles described herein apply equally to a system such as that in Ref. 2, wherein a variable retarder is used in place of the quarter-wave plate or optical compensator. The variable retarder would take on the modulation function of the piezoelectric actuator, as discussed in the section entitled **Modulation**.

CCD's have a finite electron well-capacity, and consequently, sensitivity will be greatest when the ratio q/Q is maximized, where q = number of electrons attributed to the EO signal and Q = total number of electrons. Assuming that the number of electrons in each pixel is linearly proportional to the incident radiant flux,

$$Q \propto I_d, \qquad (7a)$$

and

$$q \propto \Delta I_{EO} \equiv I_d - I_d\Big|_{\Delta\Gamma_{EO}=0}, \qquad (7b)$$

where ΔI_{EO} is the intensity contribution from the EO effect alone. Combining Eqs. (4), (5), (7a), and (7b) yields

$$\frac{q}{Q} = \frac{\cos 2\left(\Gamma_0 + \Delta\Gamma_{EO}\right) - \cos 2\left(\Gamma_0\right)}{p + \cos 2\left(\Gamma_0 + \Delta\Gamma_{EO}\right)}, \qquad (8)$$

where

$$p \equiv \frac{1 + \alpha + b}{2\sqrt{\alpha}}. \qquad (9)$$

In the small-signal limit, Eq. (8) becomes

$$\frac{q}{Q}\bigg|_{\text{Lim}\,\Delta\Gamma_{EO}\to 0} = f\left(p, \Gamma_0\right)\Delta\Gamma_{EO}, \qquad (10a)$$

where

$$f(p, \Gamma_0) \equiv \left[\frac{2\sin(2\Gamma_0)}{p + \cos(2\Gamma_0)} \right]. \qquad (10b)$$

Equation (10a) describes the fraction of electrons in each pixel attributed to the EO effect. We now consider how to use this information to optimize the system sensitivity.

Figure 69.32(a) presents a plot of Eq. (9), and Fig. 69.32(b) shows $f(p, \Gamma_0)$ defined in Eq. (10b) for the nonideal case $p = 1.05$. From Fig. 69.32(b), we see that $f(p, \Gamma_0)$ has two points for which the amplitude is a maximum. We wish to find Γ_0^{opt}— bias points for which this function is optimized. To do so, we take the derivative of $f(p, \Gamma_0)$ with respect to Γ_0, equate to zero, and solve

$$\Gamma_0^{\mathrm{opt}}(p) = \frac{1}{2}\cos^{-1}(-p^{-1}). \qquad (11)$$

Equation (11), plotted in Fig. 69.32(c), shows a distinct Γ_0 that maximizes q/Q. Therefore, we wish to optically bias the interferometer at this point, about which the small EO signal is superimposed. We note that for an ideal interferometer $p = 1$, giving $\Gamma_0^{\mathrm{opt}} = \pi/2$ where the derivative of Eq. (6) is zero. This conclusion is very different from wide-bandwidth detectors used in point sampling that achieve maximum sensitivity when $\Gamma_0 = \pi/4$, where the derivative of Eq. (6) is maximized, as explained in Ref. 2. In the general case of a nonideal interfer-

ometer, two solutions exist [as originally expected from Fig. 69.32(b)], one on either side of $\pi/2$.

Substituting Eq. (11) into Eq. (10b), we find

$$f(p, \Gamma_0)\Big|_{\Gamma_0 = \Gamma_0^{\mathrm{opt}}} = \frac{2}{p\sqrt{1 - p^{-2}}} \equiv f^{\mathrm{opt}}(p). \qquad (12)$$

The factor $f^{\mathrm{opt}}(p)$ is also plotted in Fig. 69.32(c). It has the greatest value for an ideal interferometer and decreases as we depart from ideal.

Until now, we have ignored sources of optical phase-front distortions to the probe beam. Each optical component has a finite surface accuracy and refractive index inhomogeneities. These inaccuracies are stationary in time, and spatially random, so the cumulative error is the rms combination of all components. These errors will make it impossible to achieve optimum system sensitivity at every pixel simultaneously, but two observations can be made:

1. As the region-of-interest (ROI) is decreased (within diffraction limits), the magnitude of phase distortions will decrease, and

2. As a system, sensitivity will be maximized when the average optical bias point in the ROI corresponds to the optimum bias conditions.
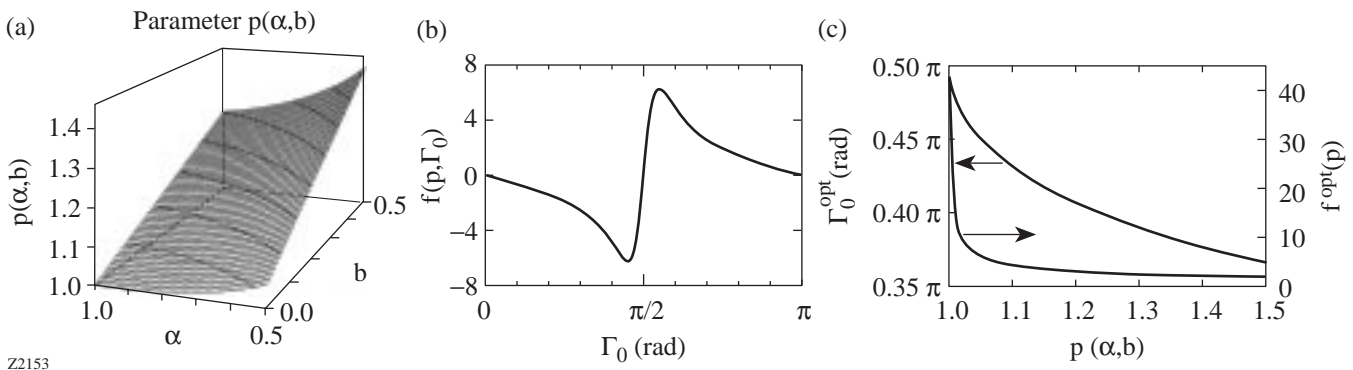

Figure 69.32

(a) Parameter $p(\alpha, b) = 1$ for an ideal interferometer and increases as (α, b) depart from ideal. (b) Sensitivity factor $f(p, \Gamma_0)$ for an arbitrary nonideal interferometer $(p = 1.05)$ has two peaks, corresponding to optimum operating bias points Γ_0^{opt}. (c) Optimum optical bias points Γ_0^{opt} and sensitivity factor $f^{\mathrm{opt}}(p)$ can be determined knowing p.

We have shown that there exists an optimum bias point about which we must modulate our signal. To determine this bias point, we must understand the origins of α and b and estimate their magnitudes.

In an ideal interferometer, the beam splitter would be infinitely thin, so that reflections occur only at one surface. Pellicle beam splitters are thin but are subject to acoustic and mechanical vibrations, making them unsuitable for this application. A thick beam splitter is more stable, but reflections from the second surface must be eliminated. Coated optics are an option, but we chose to eliminate unwanted reflections by using a wedged window. The beam is incident at Brewster's angle at the first surface such that reflectivity of p-polarized radiation is zero. The beam splitter then behaves ideally, i.e., $\alpha = 1.0$.

Background illumination, factor b in Eq. (4), is radiation collected by the detector that does not contribute to the desired signal. Fresnel reflections occur at each dielectric interface (window or lens), as in Fig. 69.33(a). Each transmitted beam is the superposition of many reflections. Beams that experience multiple reflections will be delayed more than the duration of the probe pulse, so will not interfere. To estimate b_{lens}, we compare the intensity of transmitted light delayed by more than $n_1 t$ to that delayed by exactly $n_1 t$. For a system of M windows and lenses,

$$b_{\text{lens}} = \left(1 - R^2\right)^{-M} - 1. \qquad (13)$$

Since system sensitivity decreases with increasing b, it is advantageous to minimize the reflection coefficient R at each optical element by using coated optics. A conservative estimate for the system shown in Fig. 69.31 (not all optics shown) having seven uncoated BK-7 windows ($R = 0.04$) gives $b_{\text{lens}} \cong 1.2\%$.

Fresnel reflections occur also at the surface of the crystal. Most EO materials used for sampling have a large refractive index, giving large reflections. The following expression for background contributions from the crystal, b_{EO}, is evident from Fig. 69.33(b):

$$b_{\text{EO}} = 1 - \left(1 - R_{\text{EO}}\right)^{-2}. \qquad (14)$$

Reflections from the top surface of the crystal are potentially the most detrimental to system performance. Uncoated

LiTaO$_3$ has $R_{\text{EO}} \cong 14\%$, making $b_{\text{EO}} \cong 26\%$; anti-reflection (AR) coatings, which make $R_{\text{EO}} \cong 0.03$, yield $b_{\text{EO}} \cong 6\%$. R_{EO} also effectively reduces α to α' by

$$\alpha' = \frac{I_{\text{DUT}}}{I_{\text{ref}}}\left(1 - R_{\text{EO}}\right)^2 = \alpha\left(1 - R_{\text{EO}}\right)^2, \qquad (15)$$

since only a fraction of the incident pulse makes exactly one round-trip through the crystal.

Uncoated LiTaO$_3$ makes $\alpha' = 0.74\ \alpha$, whereas coated LiTaO$_3$ produces $\alpha' = 0.94\ \alpha$. To minimize these detrimental effects, the crystal requires a nearly perfect AR coating on the first surface ($R_{\text{EO}} = 0$) and a perfect HR coating ($R = 1$) on the second surface.

The final source of background is the light reflected by the DUT from the fiber-coupled beam used to trigger the photoconductive switch. A conservative estimate assumes that the fiber is positioned at the DUT and pointed directly toward the interferometer beam splitter [Fig. 69.33(c)]. The results of this analysis will be at least an order of magnitude too large because the estimate neglects the following facts:

(1) the fiber is directed toward the DUT and will shadow reflected light;

(2) the DUT will absorb incident photons;

(3) the polarizing filter will attenuate reflected (scattered) light that is depolarized; and

(4) the photoconductive switch may be located outside the image area.

From the above argument, the results of the following simplified analysis will be reduced by a factor of 10.

The divergence angle of the beam is determined by the fiber diameter and wavelength. A fraction of the light is reflected off the beam splitter toward the camera. The distance between the relay lens and DUT is determined by the desired magnification m and lens focal length f. The lens has a finite aperture and collects only a fraction of the diverging beam from the fiber, b_{fiber}. Assuming a gaussian beam from the fiber tip, this simplified approach yields

$$b_{\text{fiber}} \approx \frac{I_{\text{ex}} R_{\text{bs}}}{I_{\text{ref}}}\operatorname{erf}\left(\frac{D}{D'}\right), \qquad (16a)$$
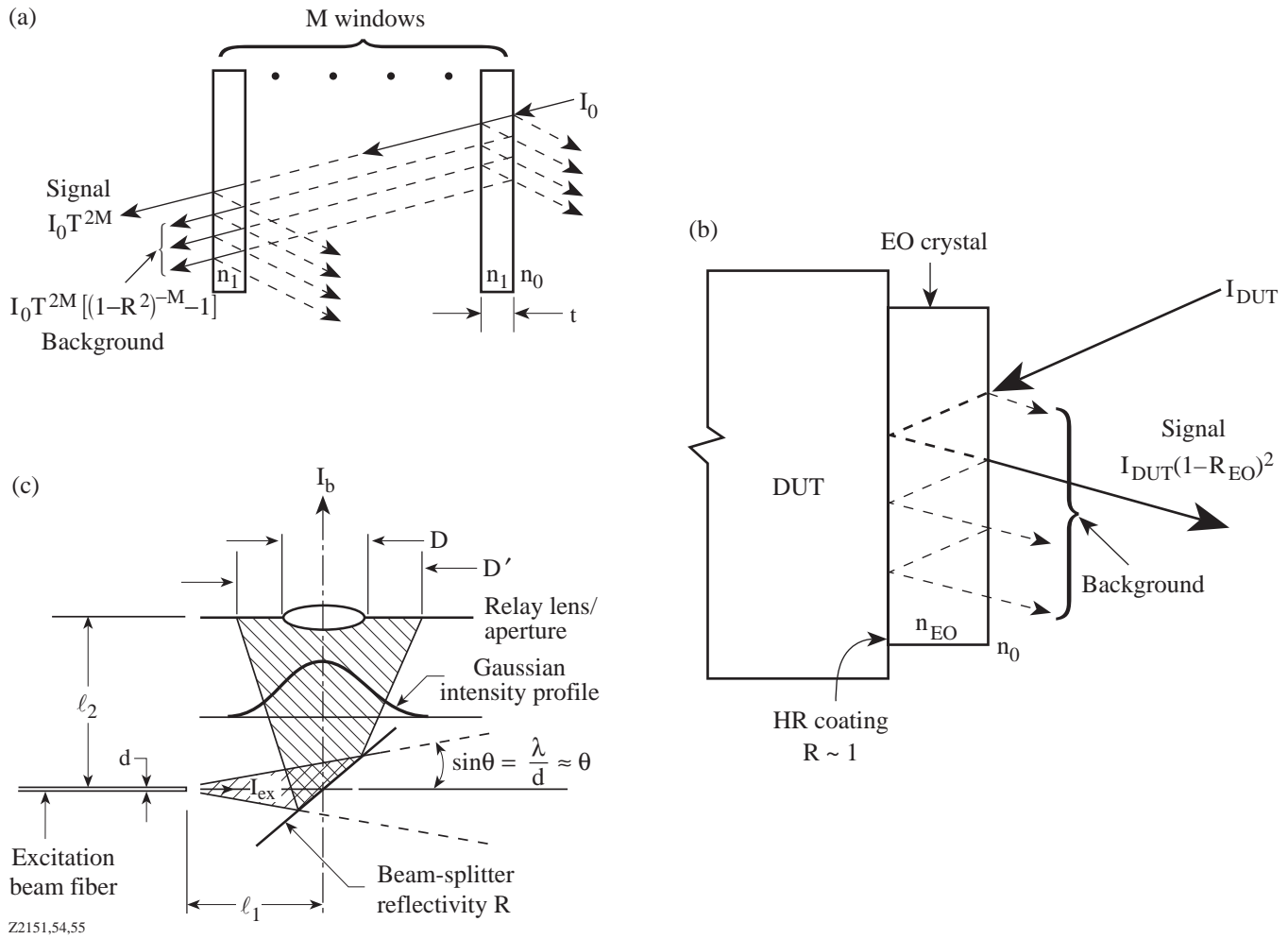
Figure 69.33
Factors that degrade interferometer performance: (a) multiple reflections from windows and lenses [R = intensity reflection coefficient, T = intensity transmission coefficient = $(1-R)$], (b) Fresnel reflections at the surface of the EO crystal, and (c) light escaping from excitation fiber.

where

$$\frac{D}{D'} = \frac{\lambda \, Dm}{2df\,(m+1)} \qquad (16b)$$

and where I_{ex} = intensity of the excitation pulse (≈ 1 mW), $I_{ref} \approx 10\ \mu$W (for pixel saturation), R_{bs} = beam-splitter reflectivity, erf( ) is the error function, D = lens-aperture diameter, D' = $1/e$ beam diameter at the lens, λ = wavelength, and d = fiber-core diameter.

Clearly, R_{bs} and m should be minimized, and f should be large. From Eqs. (16a) and (16b), typical operating condi-

tions give $b_{fiber} \cong 13\%$, which we reduce to 1.3%, as discussed above.

We have considered several factors that contribute to the nonideal terms α and b in the interferometer transfer function. It is essential to use precision optics and minimize front-surface reflections from the EO crystal to prevent system degradation. Proper adjustment of the excitation beam intensity and fiber placement will limit background contributions from the excitation source. Finally, coated optics will reduce multiple reflections from other system optics. For a well-designed system having an AR-coated crystal, we obtain $b = b_{EO} + b_{fiber} + b_{lens} \cong 0.06 + 0.012 + 0.013 = 0.085$, and $\alpha = 0.94$, thus making $p \cong 1.044$. This value for p will be used in the remaining discussion.

System Linearity and Sensitivity

Linearity of the measurement system can be derived from the ratio of Eqs. (10a) and (8), where Γ_0 is replaced with Γ_0^{opt}, and $\Delta\Gamma_{EO}$ is a small-signal perturbation about Γ_0^{opt}. Evaluating linearity at $p = 1.044$, one can show that the measured response is linear within ±5% for $\left|\Delta\Gamma_{EO}\right| < 0.015$ rad; this is more than adequate for expected signals.

We have obtained an expression for the optimum sensitivity factor $f^{opt}(p)$ and numerical estimates of the parameter p. The next step is to determine the measurement resolution of the system given this information. First, we determine the system dynamic range (DR) and minimum resolvable phase change, then the voltage and E-field needed to produce this phase change.

From Eq. (10), we can determine DR_{signal} if we assume that the pixel is nearly saturated so that $Q \approx Q_{well}$. The CCD has an electronic noise-equivalent signal $q_{eq} = 30$ electrons, shot noise $q_{shot} = 40$ electrons, and well capacity $Q_{well} = 80 \times 10^3$ electrons.[9] Setting $q_{noise} = \left(q_{eq}^2 + q_{shot}^2\right)^{1/2} = 50$ electrons, we find

$$DR_{signal} = 20 \cdot \log\left(\frac{Q_{well}}{q_{noise}} \frac{q}{Q}\right)\Bigg|_{\frac{q}{Q} = f^{opt}(p)\Delta\Gamma_{EO}}. \qquad (17)$$

For $\Delta\Gamma_{EO} = \pm 0.015$ rad (the limit of "linear" range) and $p = 1.044$, we find $f^{opt}(p) = 6.25$, and $DR_{signal} = 43$ dB.

The minimum detectable signal $\Delta\Gamma_{EO}^{min}$ is that which makes $q/Q = q_{noise}/Q_{well}$:

$$\Delta\Gamma_{EO}^{min} = \left(\frac{q_{noise}}{Q_{well}\, f^{opt}(p)}\right), \qquad (18)$$

which gives $\Delta\Gamma_{EO}^{min} = 100$ μrad, corresponding to $\lambda/6 \times 10^4$ resolution.

We relate $\Delta\Gamma_{EO}^{min}$ to the voltage necessary to produce it, using Eqs. (3c) and (3d):

$$\Delta\Gamma_{EO}^{min} \cong \frac{\pi}{\lambda} n_z^3\, r_{33}\left(\frac{\varepsilon_{sub}}{\varepsilon_{EO}}\right)\left(V^{gap,min}\right). \qquad (19)$$

The minimum detectable voltage $V^{gap,min}$ is constant for any (coplanar) gap geometry. $E_z^{surface,min}$ is the minimum field,

which, if present at the surface of the crystal, could be resolved by the system:

$$E_z^{surface,min} = \frac{V^{gap,min}}{g}. \qquad (20)$$

When testing a device fabricated on silicon ($\varepsilon_{sub} = 11.9$) using LiTaO$_3$ ($\varepsilon_{EO} = 43$, $r_{33} = 33$ pm/V, $n_z = n_e = 2.180$),[7] and $\lambda = 800$ nm, we find $\Delta\Gamma_{EO}^{min} = 3.7 \times 10^{-4}\, V^{gap,min}$. By equating $\Delta\Gamma_{EO}^{min}$ to 100 μrad, $V^{gap,min} = 270$ mV, which corresponds to 27 kV/m on a 10-μm gap.

This sensitivity is well suited to measurement of microwave devices and complex transmission line structures. Several enhancements can be made to improve suitability for digital applications. A nonlinear organic salt known as DAST has $\varepsilon_{EO} = 7.0$, Pockels coefficient $r_{11} = 160$ pm/V, and $n = 2.460$.[10] From Eq. (19), this would increase sensitivity by a factor of 43. Cooling the sensor reduces shot noise so that $q_{noise} \cong q_{eq}$, thus by Eq. (18), increasing sensitivity by a factor of 1.6. In combination, these produce $V^{gap,min} \cong 4$ mV, and $E_z^{surface,min} \cong 400$ V/m.

Modulation

Having discussed the attributes of an integrating detector, we now show how the signal is modulated about the desired operating bias point. We first discuss how the signal is modulated in each image and the timing required. We then discuss the characteristics of a frame transfer sensor and how to use these characteristics to our advantage.

Figure 69.34(a) is an expanded view of Eq. (6), about $\pi/2$. In the absence of an electric field, points A and B have equal intensity when the optical bias is adjusted to $\pm\Gamma_0^{opt}$ by displacing the reference mirror. When an E-field is present on the DUT, the resulting EO phase shift is added to the optical bias. This causes the intensity at point A to increase to C, while that at point B decreases to D. Analysis of the data is achieved by subtracting field D from B, and C from A.

The data-acquisition system is synchronized to the camera's pixel and field clocks and acquires images with the timing shown in Fig. 69.34(b). The electrical bias on the device's photoconductive switch is synchronously modulated at the 30-Hz camera field clock frequency, thus decreasing $1/f$ noise (both laser and mechanical vibrations of the interferometer). The reference mirror position is modulated at 1/2 the bias frequency. A trigger pulse generated on the mutual rising edge of bias and actuator signals triggers the digitization of
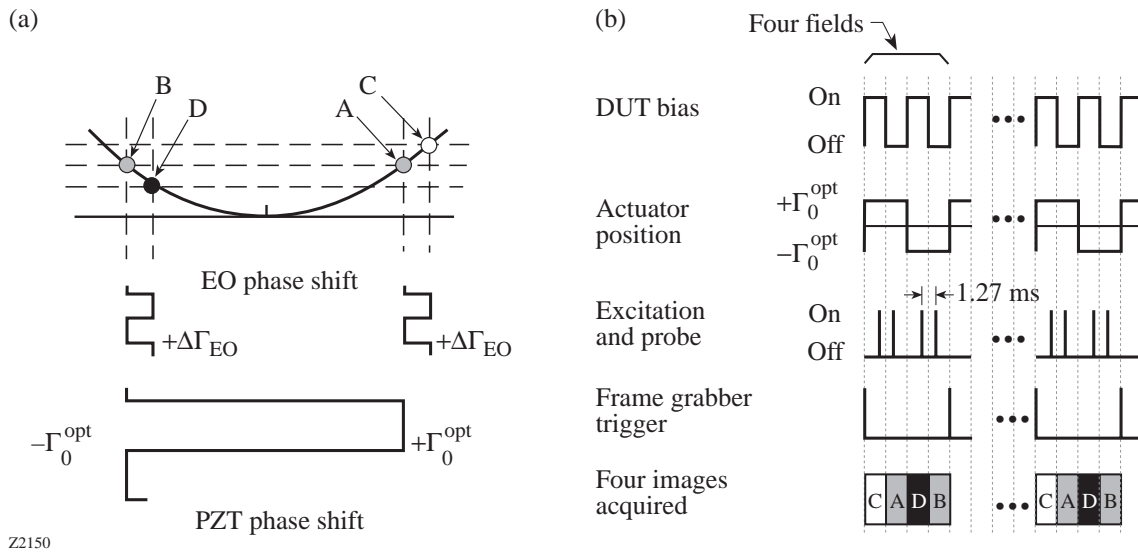
Figure 69.34

Modulation: (a) expansion of Eq. (6) about an interferometric null showing EO modulation about $\pm\Gamma_0^{opt}$ bias points, (b) modulation and image capture timing diagram.

four consecutive fields, corresponding to points C, A, D, B in Fig. 69.34(a).

The frame transfer CCD has two discrete sensor regions: an active-pixel site and a storage site of equal size. Each field is acquired over a 1/60-s integration period. An advantage of using a detector with a 1/60-s integration period is that 60-Hz electrical noise will average to zero. During integration, the active pixels integrate charge proportional to photon flux, while electrons in the storage site are clocked to the output amplifiers. During frame transfer, charges in the active pixels are transferred vertically via "bucket brigade" into the storage site. Charge transfer causes slight smearing due to transfer inefficiency, and distortion occurs for charge packets that are transferred through brightly illuminated pixels.

A high-speed modulator "gates" the laser "on" immediately before and after alternate frame transfer cycles, and "off" at all other times. This eliminates charge smearing during frame transfer and reduces the effective laser- and vibration-noise bandwidth significantly. The limiting speed for this modulation is governed by the frame transfer period (1.27 ms for our camera). If the laser is gated "on" for ~100 pulses, the effective modulation frequency would be ~750 Hz.

Summary

We have described and analyzed an ultrafast EO imaging system that uses an interferometer and CCD detector to map 2-D electric fields on an optoelectronic device. It is comparable to an ultrafast sampling oscilloscope having more than 180,000 channels. Limitations caused by using an integrating detector are reviewed, and optimum operating conditions are identified. Techniques are presented that allow modulation of the signals at 750 Hz, which will reduce sensitivity to laser and mechanical 1/f noise. System sensitivity in the absence of laser noise is estimated to be 270 mV, corresponding to 27 kV/m for a 10-μm coplanar structure. These values make the system well suited for testing microwave devices. Sensor cooling and the use of alternative EO materials should improve sensitivity by factors of 1.6 and 43, respectively, making the minimum resolvable voltage 4 mV. The system would then be easily capable of digital (e.g., CMOS) circuit evaluation.

ACKNOWLEDGMENT

REFERENCES

1. J. A. Valdmanis, G. Mourou, and C. W. Gabel, Appl. Phys. Lett. **41**, 211 (1982).

2. J. M. Wiesenfeld, IBM J. Res. Develop. **34**, 141 (1990).

3. K. E. Meyer and G. A. Mourou, in *Picosecond Electronics and Optoelectronics*, edited by G. A. Mourou, D. M. Bloom, and C. H. Lee (Springer-Verlag, New York, 1985), pp. 46–49.

4. W. Mertin, Opt. Quantum Electron. **28**, 801 (1996).

5. W. R. Donaldson, L. Kingsley, M. Weiner, A. Kim, and R. Zeto, J. Appl. Phys. **68**, 6453 (1990).

6. R. A. Falk *et al.*, in *Ninth IEEE International Pulsed Power Conference,* Digest of Technical Papers, edited by K. R. Prestwich and W. L. Baker (IEEE, New York, 1993), Vol. 1, pp. 88–91.

7. A. Yariv and P. Yeh, *Optical Waves in Crystals: Propagation and Control of Laser Radiation* (Wiley, New York, 1984), pp. 220–245.

8. D. H. Auston and M. C. Nuss, IEEE J. Quantum Electron. **24**, 184 (1988).

9. *Area Array Image Sensor Products Data Book*, Texas Instruments (1994), pp. 2-135–2-151.

10. Molecular Optoelectronics Corporation, 877 25th St. Watervliet, NY, 12189. DAST has a different Pockels coefficient matrix than the <3 m> point group, so substituting r_{11} for r_{33} is an approximation.